

Alma Mater Studiorum Università di Bologna
Archivio istituzionale della ricerca

Insight on Chirality Encoding from Small Thiolated Molecule to Plasmonic Au@Ag and Au@Au Nanoparticles

This is the final peer-reviewed author's accepted manuscript (postprint) of the following publication:

Published Version:

Carone A., Mariani P., Desert A., Romanelli M., Marcheselli J., Garavelli M., et al. (2022). Insight on Chirality Encoding from Small Thiolated Molecule to Plasmonic Au@Ag and Au@Au Nanoparticles. ACS NANO, 16(1), 1089-1101 [10.1021/acsnano.1c08824].

Availability:

This version is available at: <https://hdl.handle.net/11585/849116> since: 2023-01-16

Published:

DOI: <http://doi.org/10.1021/acsnano.1c08824>

Terms of use:

Some rights reserved. The terms and conditions for the reuse of this version of the manuscript are specified in the publishing policy. For all terms of use and more information see the publisher's website.

This item was downloaded from IRIS Università di Bologna (<https://cris.unibo.it/>).
When citing, please refer to the published version.

(Article begins on next page)

This is the final peer-reviewed accepted manuscript of:

Carone, A.; Mariani, P.; Désert, A.; Romanelli, M.; Marcheselli, J.; Garavelli, M.; Corni, S.; Rivalta, I.; Parola, S. Insight on Chirality Encoding from Small Thiolated Molecule to Plasmonic Au@Ag and Au@Au Nanoparticles. ACS Nano 2022, 16 (1), 1089–1101.

The final published version is available online at:
<https://doi.org/10.1021/acsnano.1c08824>.

Terms of use:

Some rights reserved. The terms and conditions for the reuse of this version of the manuscript are specified in the publishing policy. For all terms of use and more information see the publisher's website.

This item was downloaded from IRIS Università di Bologna (<https://cris.unibo.it/>)

When citing, please refer to the published version.

Insight on chirality encoding from small thiolated molecule to plasmonic Au@Ag and Au@Au nanoparticles

Antonio Carone,¹ Pablo Mariani,¹ Anthony Désert*,¹ Marco Romanelli,^{2,3} Jacopo Marcheselli,^{4,5} Marco Garavelli,⁴ Stefano Corni,^{2,3} Ivan Rivalta,^{1,4} Stephane Parola¹

¹ Université de Lyon, École Normale Supérieure de Lyon, Université Lyon 1, CNRS UMR 5182, Laboratoire de Chimie, 46 allée d'Italie, F-69364 Lyon, France.

² Dipartimento di Scienze Chimiche, Università di Padova, 35131 Padova, Italy.

³ Istituto di Nanoscienze, Consiglio Nazionale delle Ricerche CNR-NANO, 41125 Modena, Italy.

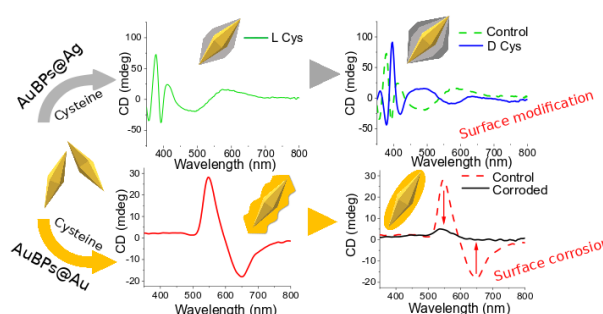
⁴ Dipartimento di Chimica Industriale "Toso Montanari", Università degli Studi di Bologna, Viale del Risorgimento 4, I-40136 Bologna, Italy.

⁵ SISSA—Scuola Internazionale Superiore di Studi Avanzati, Via Bonomea 265, 34136 Trieste, Italy.

*anthony.desert@ens-lyon.fr

ABSTRACT

Chiral plasmonic nanomaterials exhibiting intense optical activity are promising for numerous applications. In order to prepare those nanostructures, one strategy is to grow metallic nanoparticles in the presence of chiral molecules. However, in such approach the origin of the observed chirality remains uncertain. In this work, we expand the range of available chiral plasmonic nanostructures and we propose another vision of the origin of chirality in such colloidal systems. For that purpose, we investigated the synthesis of two core-shell Au@Ag and Au@Au systems built from gold nanobipyramid cores, in presence of cysteine. The obtained nanoparticles possess uniform shape and size and show plasmonic circular dichroism in the visible range, and were characterized by Electron Microscopy, Circular Dichroism and UV-Vis-NIR spectroscopy. Opto-chiral responses were found to be highly dependent on the morphology and the plasmon resonance. It revealed (i) the importance of the anisotropy for Au@Au nanoparticles and (ii) the role of the multipolar modes for Au@Ag nanoparticles on the way to achieve intense plasmonic circular dichroism. The role of cysteine as shaping agent and as chiral encoder was particularly evaluated. Our experimental results, supported by theoretical simulations, contrast the hypothesis that chiral molecules entrapped in the nanoparticles determine the chiral properties, highlighting the key role of the outmost part of the nanoparticles shell on the plasmonic circular dichroism. Along with these results, the impact of enantiomeric ratio of cysteine on the final shape suggested that the presence of a chiral shape or chiral patterns should be considered.



keywords: Chirality, Plasmon, Metal nanoparticles, Bipyramids, Core-shell

If chemists traditionally deal with chirality for organic molecular compounds, the community shows an increasing interest in chiral inorganic nanostructures.¹⁻³ Indeed, in addition to take part in fundamental understanding of chirality concept, studies of chiral inorganic nanostructures lead to unique properties of materials –e.g. high optical activity with circular dichroism (CD) response– with concrete and direct applications in the fields of catalysis, (bio)sensing and photonics. In this context, plasmonic chiral nanostructures appear as excellent objects of investigation as highlighted by recent reviews.⁴⁻⁹ The scientific community often distinguishes intrinsic chirality when the metal nanostructure exhibits a chiral geometry from induced chirality when chiral molecules are coupled to plasmonic NPs.

Thus, top-down and nanofabrication methods have enabled the preparation of plasmonic nanostructures with intrinsic chirality,^{10,11} while the grafting of chiral compounds onto pre-formed plasmonic NPs has shown coupling effects leading to CD response in the plasmon resonance region.^{12,13} Colloidal assemblies of plasmonic nanospheres and nanorods thanks to chiral linkers (like DNA or amino acids) has been also extensively reported to promote both intrinsic and/or induced chirality.¹⁴⁻¹⁷

Another strategy to address chiral plasmonic NPs is to control the growth of metal NPs in presence of chiral molecules. By this way, Ki Tae Nam and coll. have demonstrated for the first time in 2018 the colloidal synthesis of gold NPs with

unambiguous chiral geometry by a seed-mediated growth method with cysteine and glutathione.¹⁸ Then, and through several studies and reviews, they have discussed the high potential of their chiral AuNPs (with high *g*-factor values up to 0.2-0.3 in suspension) and the chirality transfer mechanism during the growth of the octahedral seeds.¹⁹⁻²¹ Since then, other seed-mediated growth methods have been reported leading to plasmonic NPs with apparent chiral geometry from gold nanorods,^{22,23} nanooctopods²⁴ or nanoplates.²⁵ However, in such strategy chirality can also be observed even without an obvious chiral shape. In 2007, two possible origins were proposed by Avnir and co-workers²⁶ for the chirality in polycrystalline metal powders doped with chiral biomolecules: (i) the presence of metal cavities and surfaces chirally imprinted (intrinsic chirality); (ii) the interaction between the metal and the entrapped chiral biomolecules (induced chirality). The hypothesis of chiral footprints was later confirmed in palladium nanopowder²⁷ and platinum layer²⁸ retaining chiral properties even after removal of the chiral template molecules.

In the case of plasmonic NPs prepared by seed-mediated growth method, induced chirality related to chiral molecules entrapped at the core-shell interface or embedded in the metallic shell is often proposed. For instance, spherical Au@Ag core-shell NPs, entrapping DNA²⁹ or cysteine³⁰ within nanogaps at the Au core-Ag shell interface, have shown large CD signals. The same authors have later reported Au@AuAg yolk-shell nanorods with chiral penicillamine inside the nanogaps.³¹ Anisotropic gold cores and entrapped cysteine have been particularly studied for preparing new chiral plasmonic NPs, like Au@Cys@Ag nanorods,³² starfruit-like AuNPs,³³ overgrown Au nanorods with one or two spikes,³⁴ or more recently like Au nanobipyramids coated by silver.³⁵ In these systems, the chirality is induced by strong coupling effect between the plasmonic nanostructures and the chiral molecules through local electromagnetic field enhancement (in nanogaps or “hotspots”).

Despite the recent important work devoted to this field, the understanding of the origin of chirality in such systems remains fragile³⁶ and we propose a full investigation to bring a different vision of the origin of chirality in such core-shell systems. Based on our previous work³⁷ describing the synthesis of gold pentatwinned nanostructures with a fine control of the particles' shape, size and plasmonic properties, we propose a strategy through the controlled overgrowth of gold nanobipyramids (AuBPs) into well-defined pentatwinned Au@Ag and Au@Au NPs, in presence of cysteine. Our approach allows high homogeneity in shape and size, which appears to be decisive to obtain strong CD signal and to understand the origin of chirality. We present herein a complete study of the impact of cysteine enantiomers on the morphology and the optical properties (absorption and CD) showing that the CD response is highly dependent on the plasmon resonance modes, as also confirmed by our computational complementary analysis. The synergistic experimental and computational studies allow a deep discussion about the role of cysteine in the origin of chirality in these nanomaterials.

RESULTS AND DISCUSSION

Preparation and morphology of AuBP@Au and AuBP@Ag nanoparticles. Pentatwinned gold bipyramids (AuBPs) were employed as core in a seed-mediated growth method in presence of cysteine (Cys) as chiral encoder to obtain AuBP@metal nanoparticles with different shell compositions (Au/Ag), shapes and optical chirality properties. Having highly monodispersed AuBPs was crucial for preparing homogeneous overgrowth NPs with an intense opto-chiral response. To synthesize the AuBPs, a protocol developed recently by our group was used.^{37,38} This method allowed us to obtain highly monodispersed AuBPs, in a high concentration ($[Au^{3+}] = 15 \text{ mM}$), with a shape purity above 95%. Two different sizes of AuBPs were synthesized to be used as core (see [Paragraph S.1](#)).

The first AuBPs batch, namely AuBP84, presented a L-LSPR centered at 800 nm and a T-LSPR at 511 nm ([Figure S1a](#)) with a ratio between L-LSPR and T-LSPR bands intensities of 7. Transmission electron microscopy (TEM) statistics over 200 particles showed for AuBP84 a length of $84 \pm 6 \text{ nm}$ and a width of $26 \pm 2 \text{ nm}$ (with an aspect ratio of 3.2) ([Table T1](#) in the [Supporting Information](#)). The second AuBPs batch, namely AuBP140, presented a L-LSPR centered at 940 nm and a T-LSPR at 512 nm ([Figure S1b](#)), with a ratio between L-LSPR and T-LSPR intensities of 8. TEM statistics showed for AuBP140 a length of $140 \pm 8 \text{ nm}$ and a width of $36 \pm 3 \text{ nm}$ (with an aspect ratio of 3.9) ([Table T1](#)). Combining inductively coupled plasma (ICP) and extinction measurements, we experimentally found the molar extinction coefficient at 400 nm for both batches, similarly to what has been done for AuNRs.³⁹ The total surface, volume, and number of AuBPs for a given Au^0 concentration were then calculated with the help of TEM images ([Table T2](#) and [Figure S2](#) in the [Supporting Information](#)).

The synthesis route for the AuBP@Ag was adapted from the protocol reported by Zhuo *et al.*, which was initially developed for the preparation of AgNRs starting from AuBPs.⁴⁰ In this reaction Ag(I) chlorine-surfactant complex is reduced using ascorbic acid (AA) in presence of CTAC on the surface of AuBPs core.

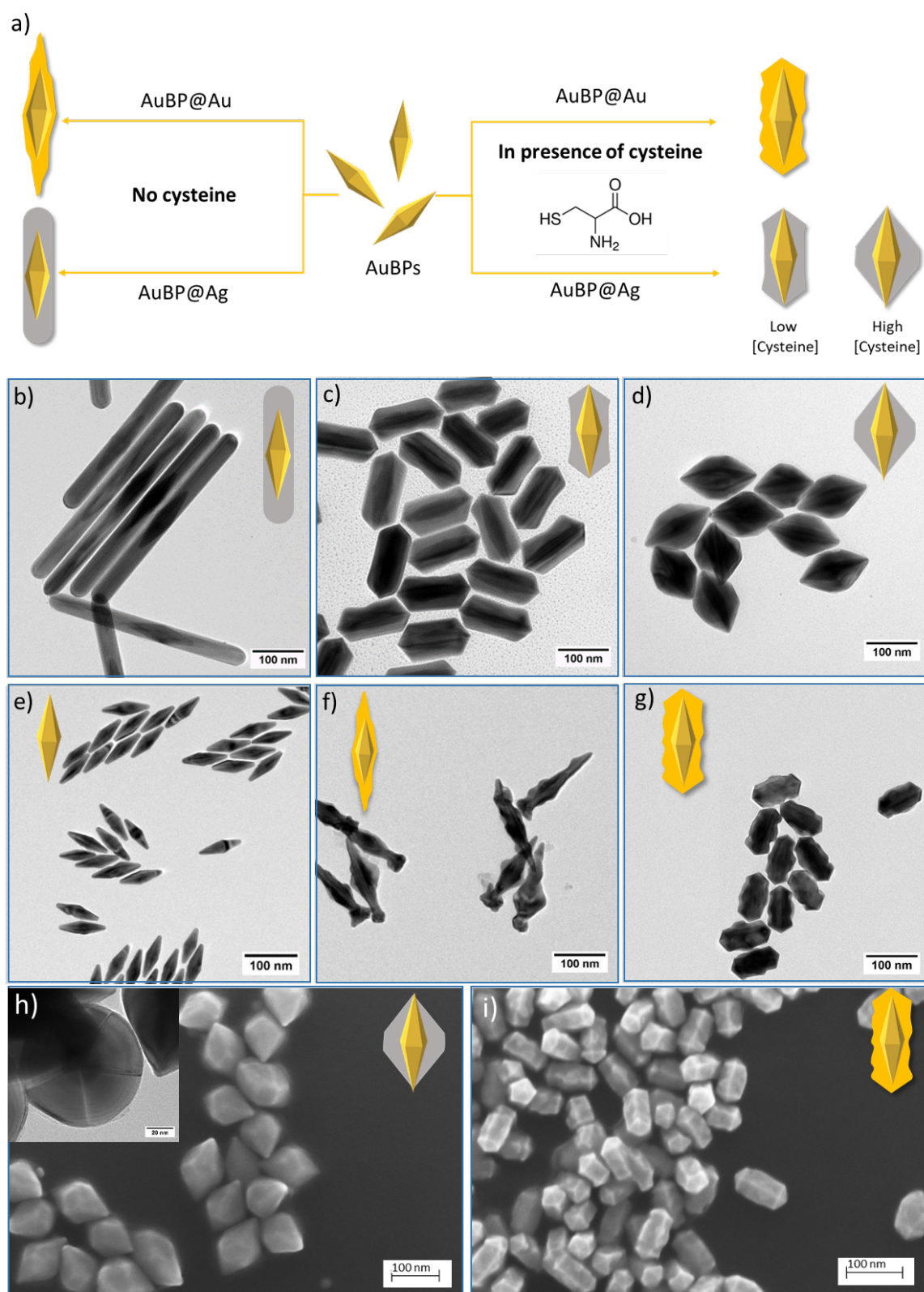


Figure 1. (a) Scheme representing the different strategies used for the preparation of the core-shell NPs, (b-g) TEM images of the obtained nanostructures in each condition. (b) AuBP140@AgNRs synthesized in absence of Cys. (c) AuBP140@Ag synthesized at 1 μM of Cys. (d) AuBP140@Ag synthesized at 5 μM of Cys. (e) Pentatwinned gold bipyramids AuBP84. (f) AuBP84@Au synthesized in absence of Cys. (g) AuBP84@Au synthesized at 10 μM of Cys. (h) SEM image of AuBP140@Ag synthesized at 20 μM . In the inset a TEM image showing the pentatwinned structure of the silver shell. (i) SEM image of AuBP84@Au synthesized at 10 μM of Cys

In order to form AuBP@Au we used another protocol that takes inspiration from the synthesis of starfruit-like nanoparticles starting from AuNRs.³³ In this case AA is used to reduce Au(III) in presence of CTAB to form Au(I) bromide-surfactant complex. The Au(I) in the complex is reduced to Au⁰ by the excess of AA on the surface of AuBPs in presence of Ag(I) as a shaping agent. In both cases, Cys was used as chiral encoder due to the ability to easily bind to Au surface through its thiol group.

It was observed that the presence of Cys in the reaction mixture led to radical change in the shells morphologies for both AuBP140@Ag and AuBP84@Au. The impact of Cys on the shape was then further studied for both systems (Figure 1a). For AuBP140@Ag system, when no Cys was present in the reaction mixture, some well calibrated AuBP140@AgNRs were formed as expected (Figure 1b). At 1 μ M Cys in the reaction mixture, the silver shell growth direction was completely reversed. The analysis of the final length (142 ± 8 nm) in the TEM images (Figure 1c) showed that the silver deposition along the longitudinal axis was completely suppressed in favor of a deposition on the side of the AuBPs (final aspect ratio of 1.9). The nanoparticles showed regular edges on the tips, while a certain degree of irregularity was present on the sides. Increasing Cys concentration ([Cys]) in the reaction mixture led again to a change in the synthesized nanoparticles morphology. While at 1 μ M Cys a truncated rod-like structure was formed, at 5 μ M Cys the Ag deposition on the side was enhanced as shown in Figure 1d (final aspect ratio of 1.4). TEM analysis confirmed the 5-fold symmetry of the metallic shell (Figure 1h) as observed for the pentatwinned core. Further increase of [Cys], *i.e.* from 5 μ M to 100 μ M, did not bring any change in the nanoparticles morphology. Similar shaping effect was observed in presence of Cys,^{33,35} using different thiolated molecules⁴¹ or DMSO^{42,43} to control the final morphology of the metallic shell. However, the low [Cys] necessary to provoke a change in morphology (1 μ M, with [Cys]/[Ag] $\approx 1 \cdot 10^{-3}$) lead to the assumption that Cys is playing a role by binding on the Au⁰ surface, rather than influencing other species in solution. We assume that Cys binding through the thiol group to the AuBPs surface is altering the growth kinetics.

A similar impact of Cys on the morphology was also observed when a Au shell was deposited around the AuBP84. When no Cys was present in the reaction mixture, the final structure showed a length of 167 ± 27 nm. Compared with the length of the AuBP84 (84 ± 6 nm), a predominant growth along the longitudinal axis is demonstrated. These irregular structures recall the morphology of nails (presence of heads and tips) with evident signs of anarchic growth (Figure 1f). At 10 μ M Cys, the deposition of the metal shell was predominant on the side, forming gnocchi-like nanoparticles with a wavy lateral surface and well-shaped facets on the tips (Figure 1g). Electron microscopy analyses (SEM, TEM and HRTEM) also confirmed that in this case the shell preserved the pentatwinned structure of the AuBPs (Figure 1i). Statistical analysis showed a length of 97 ± 5 nm, evidencing a few nanometers deposition on the AuBPs tips (final aspect ratio of 1.8). The presence of Cys permitted also to retrieve a uniformity in nanoparticles size and shape. Increasing [Cys] from 5 μ M to 20 μ M did not lead to appreciable changes in the overall morphology. Similar overgrown nanostructure is obtained by combining different surfactants⁴⁴ or using Cys and glutathione to prevent overgrowth along the longitudinal axis starting from AuNRs.⁴⁵ The formation of a wavy lateral surface observed in our gnocchi-like nanoparticles is similar to the arrow-like nanostructure formed starting from AuNRs.⁴⁶ In the same study, it was found by Wang *et al.* that Cys is active on the formation of the wavy lateral surface. The strong Au-S formed on the surface in presence of Cys is slowing the metal deposition rate and thus inducing a thermodynamic controlled growth with formation of more stable prismatic facets on the side. When a different size of AuBPs core was used, the same shaping effect in presence of Cys was found for both AuBP84@Ag and AuBP140@Au (Figure S3).

Spectroscopic characterization. When Cys was employed, a blue-shift of the L-LSPR was recorded in the extinction spectra for both AuBP84@Au and AuBP140@Ag (Figure 2a,b), reflecting the lower aspect ratio observed by microscopy. For AuBP84@Au the L-LSPR was shifted from 800 nm toward 600-630 nm (5 μ M to 40 μ M Cys) (Figure 2a). In a similar way, in AuBP140@Ag the L-LSPR was shifted from 940 nm toward 580-670 nm (1 μ M to 100 μ M Cys) (Figure 2b).

Along with the changes in the extinction spectra, when Cys was used an intense plasmonic circular dichroism (PCD) was detected for both systems (Figure 2c,d). For AuBP84@Au, at 5 μ M Cys abisignate peak appeared (Figure 2c). The positive band between 500 nm and 600 nm was attributed to the T-LSPR, while the negative band between 600 nm and 700 nm was attributed to the L-LSPR. Increasing [Cys] to 10 μ M provoked a reduction of the g-factor. When 20 μ M Cys was used the shift of the negative band between 600 nm and 650 nm was associated to the shifts of L-LSPR in the extinction spectra (Figure 2a). When 40 μ M Cys was used, a negative peak appeared at 374 nm. We attributed this peak to a previously reported chiral Cys-Au(I) complex, formed as a result of the excess of Cys able to react with available Au(I) in solution.^{33,47}

For AuBP140@Ag, the g-factor spectra (Figure 2d) changed with different [Cys], partly due to the change in the extinction spectra caused by the different morphologies. In the spectrum of AuBP140@Ag (Figure 2d), when 1 μ M Cys was employed

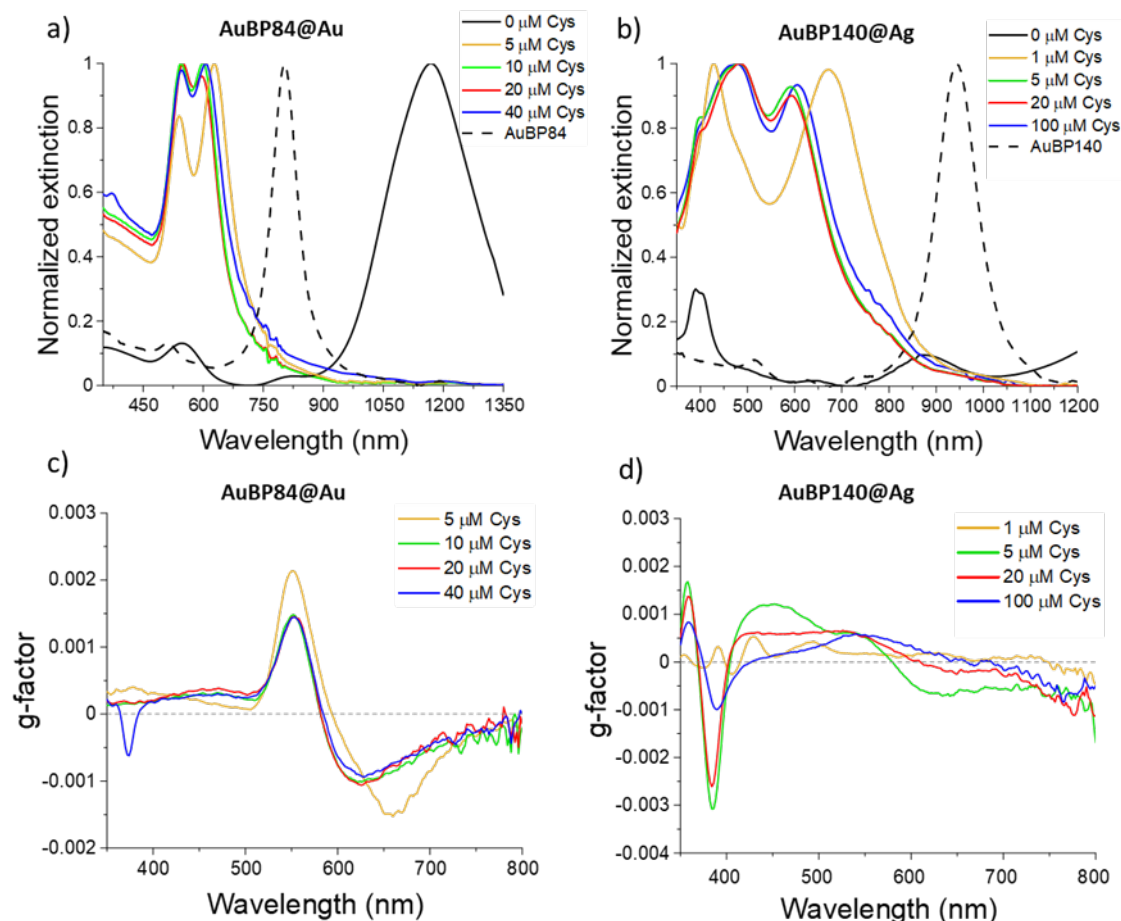


Figure 2. Effect of Cys concentration on the optical response. (a,b) Normalized extinction spectra of (a) AuBP84@Au and (b) AuBP140@Ag obtained at different Cys concentrations. (c,d) Calculated g-factor of (c) AuBP84@Au and (d) AuBP140@Ag obtained using different concentrations of Cys.

153 six broad bands with a relative low intensity were observed. When [Cys] was set from 5 μM to 20 μM, a predominant
 154 contribution in the spectrum appeared at 380 nm. When [Cys] was further increased to 100 μM, even if no relevant changes
 155 appear on the extinction spectra, the g-factor was observed to decrease.

156 For both AuBP140@Ag and AuBP84@Au systems when enantiomeric pure D-Cys or L-Cys (Figure 3a,b) was used, no
 157 difference on the extinction spectra was recorded. The CD spectra, instead, showed a mirror signal depending on the
 158 enantiomer used, confirming the role of Cys as chiral encoder. However, differently from the AuBP84@Au system, where the
 159 two contributions to the CD spectrum were easily attributed to L-LSPR and T-LSPR (Figure 3b), the CD spectra of the
 160 AuBP140@Ag feature a peculiar lineshape (Figure 3a). To identify the different contributions on the CD spectrum, the
 161 extinction spectrum of AuBP140@Ag synthesized at 20 μM Cys was simulated (Figure 3c,d) (see computational details in
 162 methods section). While blue-shifted with respect to experimental data (by <2 eV *i.e.* ~35 nm), the simulated spectra feature
 163 three main contributing bands to the extinction spectrum of AuBP140@Ag with the same morphology, *i.e.* those obtained
 164 using a [Cys] from 5 μM. As it is possible to see in Figure 3c,d the absorption peak at the highest wavelength is associated to
 165 a longitudinal plasmon band (L3) while the central peak is due to two transversal absorptions (T2, T3), one of which involves
 166 the tip of the Au core (T2). Moreover, as indicated by the surface charge distribution plots (Figure 3d), these T2, T3 and L3
 167 resonances had dipolar character, in contrast with the lowest wavelength peaks (T1, L1, L2) featuring a multipolar character
 168 for both longitudinal and transversal excitations, with T1 being more intense and showing predominant quadrupolar
 169 contribution. The presence of multipolar resonances in the low wavelength range, *i.e.* around the experimental peak at 400
 170 nm, was further confirmed by simulations of absorption spectra within a quasi-static approximation (Figure S4) and it was in
 171 agreement with other results present for similar systems.^{32,48} Notably, by simulating the absorption spectra of the Ag outer
 172 shell with (and without) the Au core (Figure S5) we observed that optical properties of the AuBP140@Ag objects were
 173 dominated by the outer Ag surface, with spectra being almost identical to those of the Ag particles, thus, with minor effects
 174 induced by the Au core. A similar analysis concerning the extinction spectrum and related surface charge densities for the

AuBP84@Au system is reported in Figure S17, showing a good agreement with experimental data and confirming the assignment of the L- and T-LSPR bands (see Figure 3b).

The CD signals for AuBP140@Ag were then attributed according to the simulated extinction spectrum. The Figure 3a showed the superposition of the extinction and CD spectra along with the different attributions for AuBP140@Ag synthesized at 20 μ M Cys. The band centered at 630 nm in the CD spectrum was attributed to the L-LSPR (L3) while the broad band going from 400 nm to 580 nm to T2 and T3. The intense sharp peak at 380 nm was attributed to the multipolar resonances (T1, L1

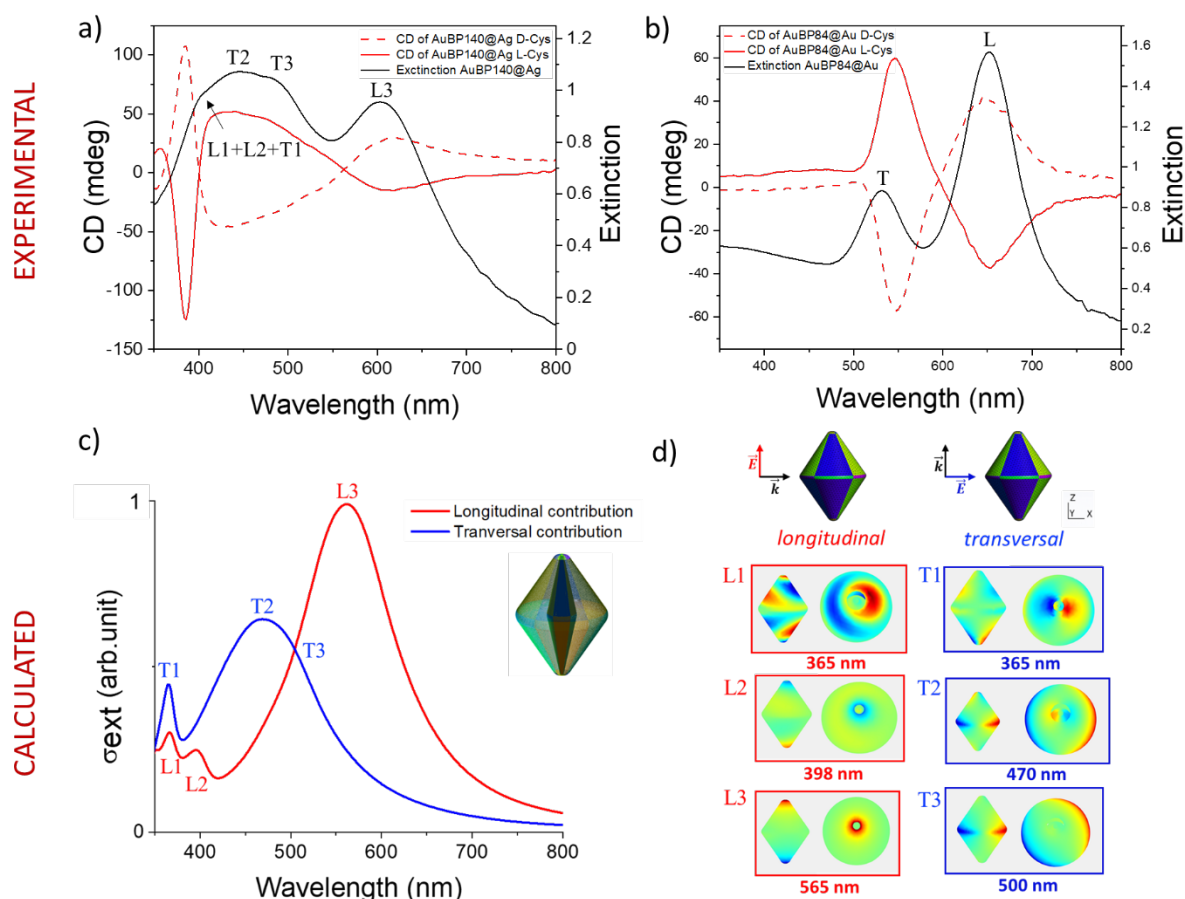


Figure 3. (a,b) Superposition of experimental extinction and circular dichroism spectra obtained in presence of L-Cys or D-Cys for (a) AuBP140@Ag and (b) AuBP84@Au. (c) Simulated extinction spectra of the AuBP140@Ag model structure due to an incident electric field oriented along either the transversal (blue curve) or longitudinal direction (red curve). The labels refer to the corresponding surface charges shown in panel d). (d) Color-scale representation of surface charge distributions induced by the EM field at selected wavelengths.

and L2) according to our theoretical calculations. The use of multipolar resonance was already suggested to be a viable way to obtain materials exhibiting a strong PCD and our results match with what predicted in the literature.⁴⁹⁻⁵¹

In order to better study the correlation between the CD and the extinction spectra we tried to vary the thickness of the metal shell for both systems (Figure 4). Thus, the initial concentration of AuBPs was varied (the concentration expressed in [Au⁰] and [NPs] can be found in the Table T2 in the Supporting Information). For instance, reducing the initial number of AuBPs resulted in a redistribution of metal atoms available to form the shell among a smaller number of AuBPs, and thus in a thicker shell. For both systems, we noted that increasing the metal shell thickness led to more isotropic particles. This was because the metal shell deposition is predominant on the lateral side of the AuBPs for both systems.

For AuBP@Au, when 80 μ L was used, statistical analysis on TEM showed a length of 95 ± 5 nm and a width of 43 ± 5 nm that can be compared with the initial AuBP84 (84 ± 6 nm long and 26 ± 2 nm wide) (Figure 4c). It was also noted the appearance of a wavy surface on the lateral side along with facets formation on the tips. When 50 μ L was used, the previously observed gnocchi-like nanoparticles were formed. Well-shaped facets along the tips as well as an evident wavy surface on

the side were observed. A measured length of 97 ± 5 nm and a width of 53 ± 3 nm evidenced how the metal deposition, once tips were formed, was continued on the sides. The wavy surface on the lateral side is less pronounced when 30 μ L was used and almost disappeared when 20 μ L was used. The TEM measurements of the objects formed at 20 μ L, 99 ± 5 nm long and 79 ± 5 nm wide, showed an almost isotropic structure. Thanks to the more symmetric geometry of the object, the preferred orientation on the TEM grid was no more on the flat side and it was possible to observe the pentagonal symmetry of the nanostructure formed (Figure 4c).

The superposition of the various extinction spectra confirmed this trend (Figure 4a). With 80 μ L being used the L-LSPR was located at 678 nm and when the number of AuBPs was decreased, the peak progressively blue shifted and merged with the T-LSPR to form one single peak located at 567 nm. The maximum of the peaks in the superposition of the various CD spectra, followed faithfully the extinction spectra (Figure 4a). The broad negative peaks between 600 nm and 700 nm moved according to the L-LSPR while the positive peaks between 500 nm and 600 nm moved along with the T-LSPR. Interestingly, when 30 μ L of AuBPs was used, the intensity of the CD diminished considerably and was almost totally suppressed at 20 μ L, condition that caused the L-LSPR and T-LSPR to merge in the extinction spectrum. The simulation carried out by Govorov *et al.*⁵² showed the importance of anisotropy in the interaction between a molecule and plasmonic nanoparticles for PCD. Annulation of PCD signal due to increasing symmetry was also already observed experimentally.³³ Being the CD peaks of opposite signs when L-LSPR and T-LSPR get closer due to the reduction of aspect ratio, they merged to one peak and the final CD was completely suppressed.

For AuBP140@Ag when 50 μ L of AuBP140 was used, a predominant deposition on the side of the AuBPs was observed (Figure 4d). The different contrast between Au and Ag on TEM allowed us to distinguish the tips of the AuBP core protruding outside the silver shell. Anyway, our simulations suggested that whether the inner AuBP was protruding outside the outer

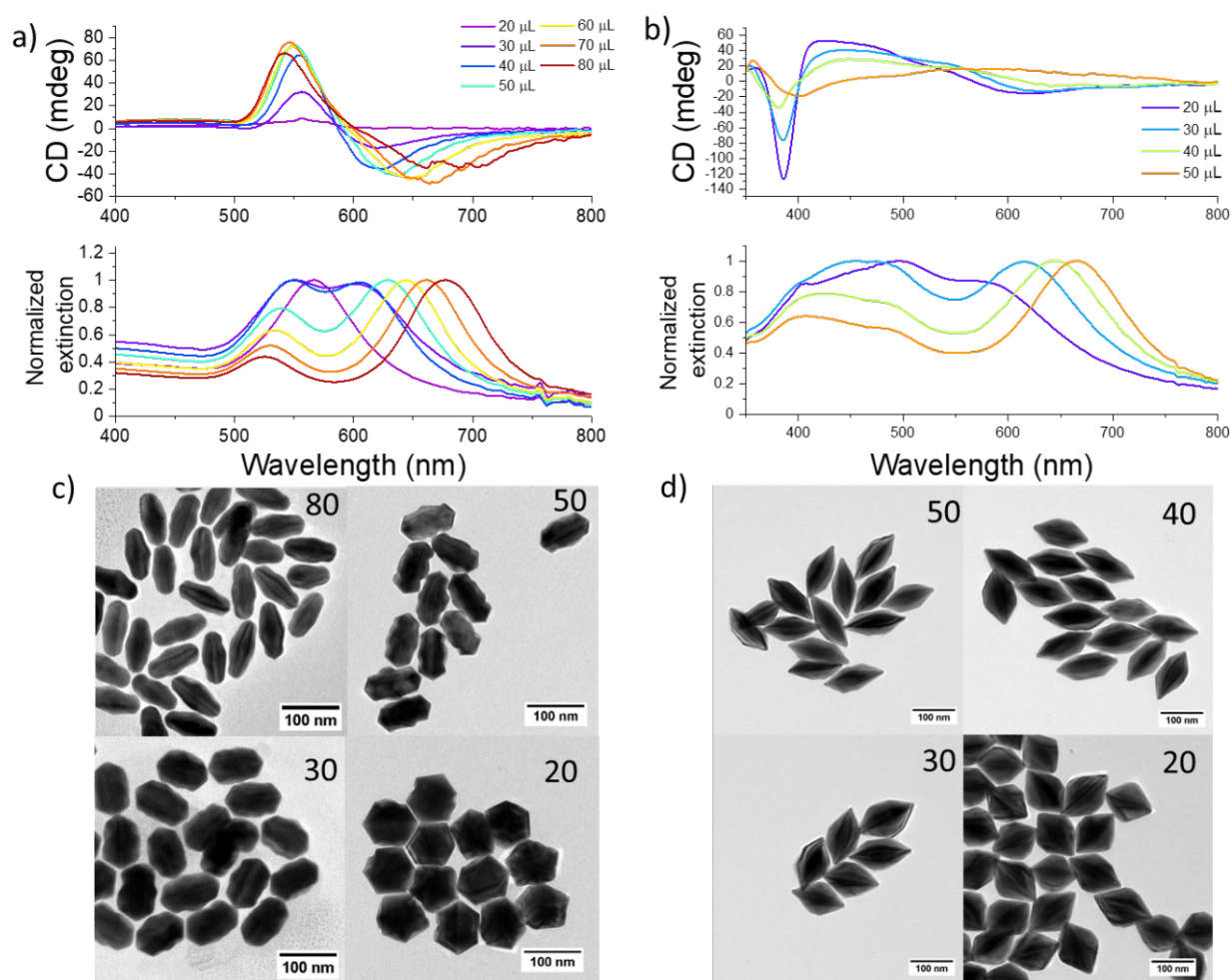


Figure 4. (a,b) Circular dichroism and extinction spectra of (a) AuBP84@Au and (b) AuBP140@Ag nanoparticles obtained by varying the volume of AuBPs suspension. (c,d) Corresponding TEM images of (c) AuBP84@Au and (d) AuBP140@Ag. The number in the upper right corner refers to the added volume in μ L of AuBPs.

shell or completely included in the silver layer, did not affect the optical response of the overall system (Figure S6). When 50 μ L, 40 μ L, 30 μ L and 20 μ L of AuBPs was used, the width of the structures changed from 58 ± 3 nm, 66 ± 4 nm, 77 ± 5 nm to 94 ± 5 nm, respectively. The length, as expected, remained equal to the length of the AuBPs used as core (140 ± 8 nm). As a consequence, the L3 was blue shifted when a minor number of AuBPs was used, moving from 650 nm (50 μ L used) to 578 nm (20 μ L used) (Figure 4b). Moreover, at 20 μ L, the T1 peak appeared at 400 nm as a shoulder of the broad band formed by merging T2 and T3 resonances.

Simulated extinction spectra of AuBP@Ag with variable aspect ratios pointed out that the decrease of aspect ratio induces a blue shift of L-LSPR and a red-shift of T-LSPR (Figure S7). Notably, the spectral position of the multipolar theoretical signal remained invariant, in agreement with the experimental trends. In the superposition of the CD spectra, the band between 600 nm and 700 nm moved accordingly to L-LSPR. Differently to AuBP@Au, for AuBP@Ag a more isotropic structure did not result in a total suppression of the CD. This was due to the apparition of a new contribution in the CD spectrum, deriving mostly from the T1 and L1 peaks. The relative high intensity of this CD peak is thus due to his multipolar character. The use of multipolar resonance was already suggested to be a viable way to obtain materials exhibiting a strong PCD⁴⁹⁻⁵¹ and it is strongly confirmed here.

Towards the origin of chirality. The dipole-plasmon coupling effect between chiral molecules grafted on the surface of the nanoparticles is a common accepted mechanism leading to PCD for plasmonic nanoparticles.^{12,13}

Moreover, Hou *et al.* advanced the hypothesis that for some core-shell systems, chiral molecules entrapped inside the NPs could be also contributing to the PCD.³² In another study of the same group, AuNR@Au starfruit-like nanoparticles obtained in presence of Cys showed no change in PCD when the L-Cys on surface was exchanged with D-Cys. Starting from this evidence, it was suggested that either Cys entrapped at the interface in-between the Au-Au core-shell, as well as the Cys distributed inside the lattice hotspots of the Au shell, could be the origin of PCD.³³ In a recently published paper,³⁵ the same idea was taken up for a AuBP@Ag system showing PCD, where the presence of sulfur atoms inside the NPs was showed by Energy Dispersive X-ray Spectrometry (EDS). Indeed, the presence of organic molecules inside metal core-shell nanoparticles is discussed in literature.^{53,54}

In our case, the lack of clear chiral shapes and the g-factor values around 0.002-0.003 (Figure 2c,d) for AuBP@Au and AuBP@Ag NPs, suggest that PCD response could result from electromagnetic coupling effect between Cys molecules and plasmonic nanostructure. In order to explore this hypothesis, the effect on PCD of Cys molecule on the surface of the NPs was evaluated. The exchange L-Cys with D-Cys on the surface was achieved but no change in the PCD was recorded (Figure S8). To corroborate this result, Cys was removed from the surface by reductive desorption reaction in presence on NaBH₄ (Paragraph S.2 in the Supporting Information).⁵⁵ Also in this case the PCD response was still present after the NaBH₄ treatment (Figure S9). The quantity of Cys released from the surface was then carefully quantified using a thiol-selective dye method already employed in literature to determine Cys on AuNPs (Figure S10).¹⁸ The quantified amounts of Cys on the surface were 9.71 ± 0.65 pmol for AuBP84@Au and 10.94 ± 0.65 pmol for AuBP140@Ag. The Cys surface density for AuBP84@Au and AuBP140@Ag was 0.0021 nmol/cm² and 0.0049 nmol/cm², respectively (Table T3 in the Supporting Information). According to these results, we can affirm that Cys grafted on the surface is not responsible of the PCD.

The role of possible Cys entrapped inside the NPs on the PCD was evaluated. However, our attempts to localize the Cys inside the NPs by NMR and EDS did not bring any significant evidence. The presence of molecules inside the nanoparticles is usually evidenced by nanogaps directly observed in the TEM images. Here, HRTEM showed a continuous core-shell structure (Figure S11, S12) without gap.

Regardless of the presence of Cys or not inside the NPs, since common explanations for core-shell systems on PCD origin could be rather incomplete, we proceeded to study its role on PCD using some conceptually simple experiments.

AuBP140@Ag nanoparticles were synthesized taking care to deposit the silver shell in two steps. A first incomplete shell was deposited in presence of L-Cys. Then, the shell deposition was completed in presence of D-Cys to form AuBP140@AgL@AgD (Figure 5a). More in detail, 30 μ L of AuBPs was employed to synthesize AuBP140@Ag-L, in standard conditions, in presence of L-Cys. Such incomplete structures are the same ones observed using 30 μ L of AuBPs in Figure 4. The so-synthesized NPs were then washed three times by centrifugation, to remove the excess of L-Cys still present in the growth solution, and re-dispersed in CTAC. Then, the silver shell deposition was completed using the same conditions as before but this time introducing D-Cys. TEM images (Figure 5c) as well as extinction spectra (Figure S13) confirmed the correct formation of the core-shell nanostructures. The CD spectrum recorded for AuBP140@AgL@AgD (Figure 5b) was almost mirror to the AuBP140@AgL@AgL (synthesized using L-Cys in both steps and used as control). The small discrepancies, like position and broadness of the peaks, were attributed to a slightly different position of the peaks in the extinction spectrum (Figure

S13). This evidence permitted to highlight the major role of the external part of the shell with respect to the inner part of the particle on the PCD properties.

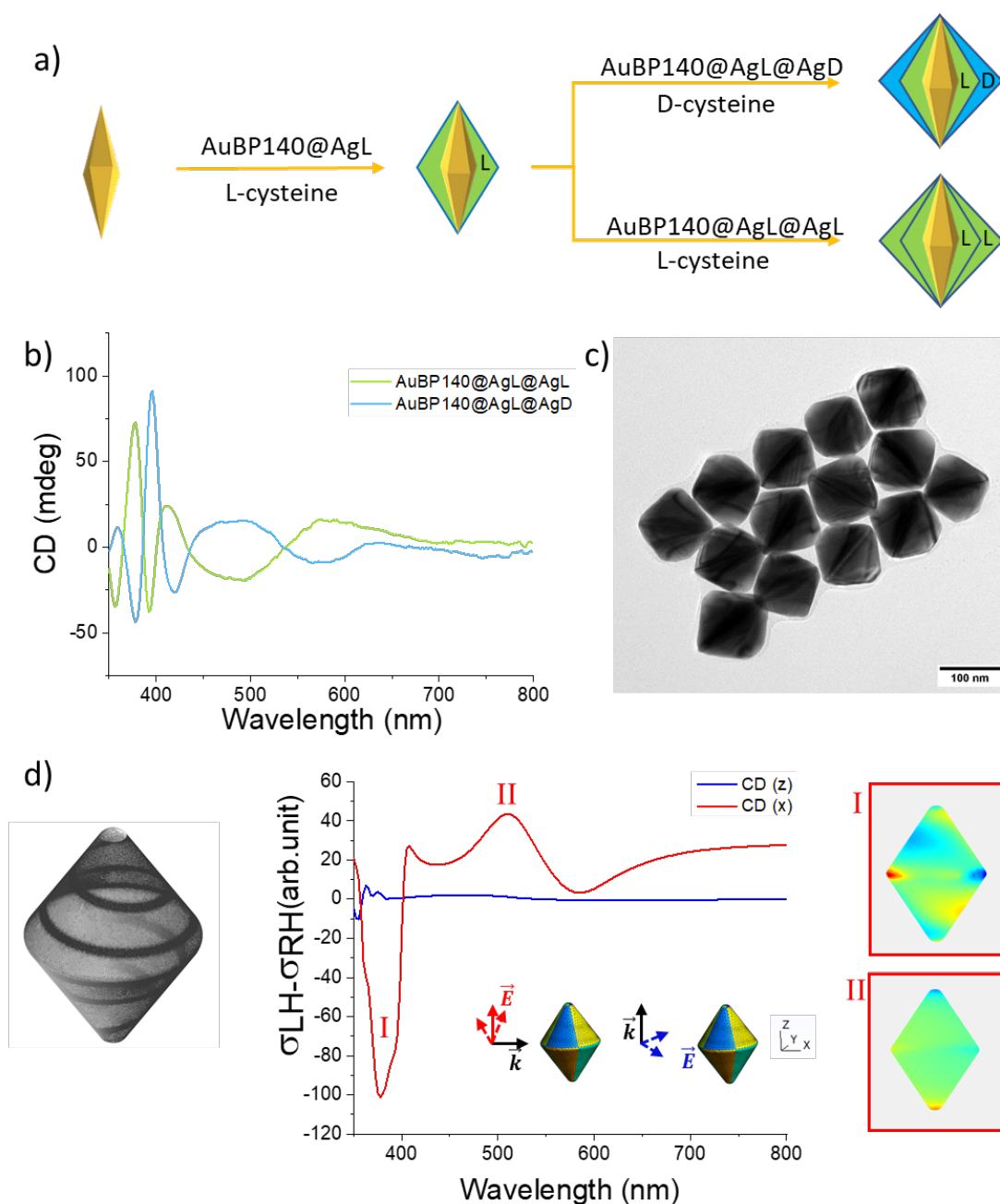


Figure 5. (a) Scheme representing the two steps synthesis with the inversion of the Cys enantiomers during the formation of the outer shell. (b) Circular dichroism spectra of the nano-objects obtained. (c) TEM image of AuBP140@AgL@AgD. (d) Simulated CD response of the chiral AuBP140@Ag model structure obtained by introducing a spiral motif on the Ag surface (shown on the left) and corresponding surface charges.

We can exclude that L-Cys entrapped in between Au core and Ag shell is at the origin of PCD as previously proposed in a similar system.³² If this was the case, the final CD spectrum of AuBP140@AgL@AgD should have shown a similar trend as AuBP140@AgL@AgL, when L-Cys was used in both steps. Moreover, a similar argumentation can be extended to exclude the possible contribution of the L-Cys entrapped inside the crystal lattice of the first silver shell, with a mechanism similar to what proposed for this system.³⁵ If the Cys entrapped inside the hotspots of the Ag crystal lattice was responsible for the PCD, having half of the silver shell formed in presence of L-Cys and the other half with D-Cys should have shown a strong impact on the final CD spectrum. From this result we can suggest that: (i) only the Cys present in hotspots near the surface contributes to PCD or (ii) a chiral shape of the particles or chiral surface patterns, difficult to visualize with routine TEM or SEM analysis,

were present. In order to evaluate the latter hypothesis from a theoretical point of view, we built a AuBP140@Ag model with a chiral surface pattern obtained numerically by thickening the external surface mesh around a spiral pattern along the longitudinal axis (Figure 5d).

As shown in Figure 5d, the simulated CD spectrum of the AuBP140@Ag model with pattern features one main peak below 400 nm (when the light electric field rotates in the z-y plane while the wave is travelling along x, see cartesian reference frame in Figure 5d) that had a multipolar character, as indicated by the charge distribution, in agreement with the multipolar signal observed experimentally (see Figure 4b). A signal with opposite sign with respect to the multipolar one is found around 500 nm, possessing a dipolar character, while transversal CD signals are absent. The simulated CD spectra, despite the crude chiral surface modeling, are in qualitative agreement with the experimental data for AuBP140@Ag particles obtained (see Figure 4b), indicating that chiral patterns present on the external Ag surface could provide PCD signals such as those obtained experimentally. Additional AuBP140Ag model structures, whose dimensions were chosen from the extreme tails of TEM

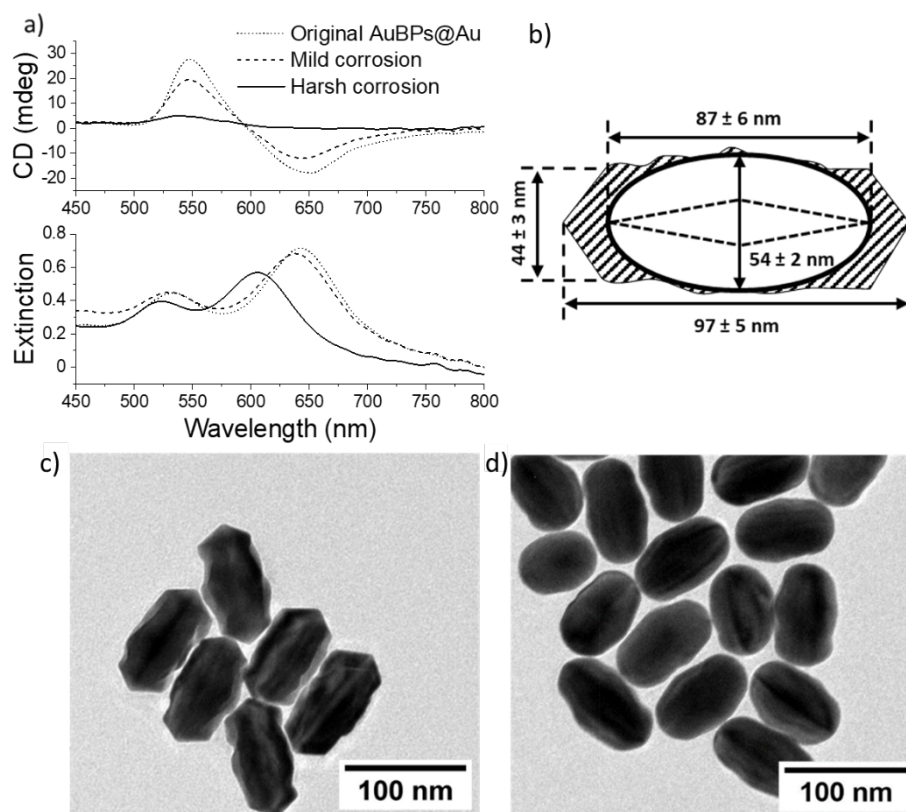


Figure 6. (a) Circular Dichroism and Extinction spectra for different corrosion conditions. (b) Schema reporting the corroded area of gold from the original AuBP84@Au. The dimensions of the inner AuBP (dashed line) and the particles after harsh corrosion (solid line) are also represented. (c,d) TEM images of (c) AuBP84@Au and (d) AuBP84@Au after harsh corrosion.

statistical distribution previously mentioned and featuring a similar spiral motif to that of Figure 5d, were considered for further calculations. The results, shown in Figure S16 in the SI, clearly indicate that the different structures present similar CD responses.

In order to corroborate this claim, the importance of the external part of the metallic shell to PCD was further investigated experimentally also in AuBP84@Au systems (Figure 6). AuBP84@Au were partially corroded to study the impact on PCD by removing the superficial Au shell. In addition, the corrosion of the surface brought inner layers of metallic shell to the surface, allowing us to study their contribution to PCD by removing the contribution of the uppermost surface. We chose tetrachloroauric acid as oxidizing agent, which is commonly employed in etching methods for smoothing gold nanoparticles.^{56,57}

Tuning the Au^{3+} quantity introduced in the reaction allowed us to have a very good control over the etching process. A first mild etching was made by adding 2.5% of $\text{Au}^{3+}/\text{Au}^0_{\text{shell}}$, at room temperature. A second harsh etching was made adding 10% of $\text{Au}^{3+}/\text{Au}^0_{\text{shell}}$ at 45 °C. As shown in Figure 6a, the mild etching resulted in a shift in the extinction spectrum of the L-LSPR

from 644 nm to 638 nm. In the CD spectrum the impact was significant with a loss of 30% of the signal intensity. When harsh conditions were used, the extinction spectrum showed a more pronounced shift of the L-LSPR from 644 nm to 604 nm followed by almost total suppression of the PCD bisignate signal.

TEM images before and after etching (Figure 6c,d) showed that the surface asperities were corroded to generate smooth structures. From statistical analysis of the lengths (see Figure 6b) it was possible to observe that the majority of the gold shell deposited was still present in the structure. The strong PCD variation intensity, when the surface was corroded, confirmed the importance of the external structured layers in the PCD. Moreover, this result suggested that Cys entrapped deep inside the metal shell hotspots, as well as Cys at the interface, was not participating to PCD. Since most part of the metal shell was still present, removing few nanometers of the surface should not have played such a significant role on the observed spectra. The importance of the superficial part of the shell on PCD led us to investigate a possible different role of Cys.

To bring in additive evidence that Cys could have an impact on the final shape, AuBP84@Ag were synthesized in presence of a racemic mixture of L-Cys and D-Cys. As expected, the CD spectrum showed the suppression of the PCD (Figure S14). More interesting and not expected was the difference in the extinction spectra when the racemic mixture was used. The NPs synthesized using pure L-Cys or D-Cys possessed nearly identical extinction spectra (Figure 7a), while when racemic Cys was used, an evident difference was present in the extinction spectrum. The TEM observation confirmed that a different shape was present depending if an enantiomeric pure Cys was used or not (Figure 7b,c). When enantiomeric pure L or D-Cys was used, the formed objects were similar to the nanoparticles described above with well-defined facets, while using racemic Cys led to the formation of more spherical particles. To the best of our knowledge the difference in reactivity was not observed elsewhere for this kind of systems and clearly bring in evidence that contribution of a chiral shape of the particles to PCD should not be excluded.

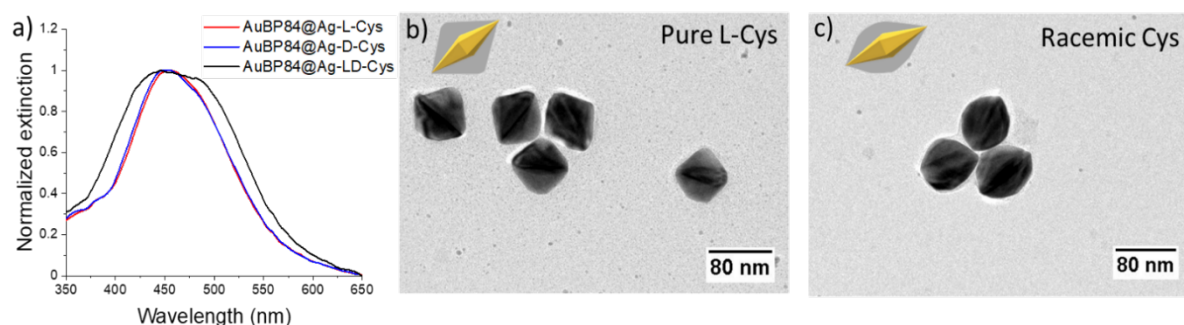


Figure 7. (a) Extinction spectra of AuBP84@Ag obtained with L, D or racemic Cys. (b,c) TEM images of AuBP84@Ag obtained with (b) pure L-cys and (c) a racemic mixture of Cys.

CONCLUSIONS

In this work we present AuBP@Au and AuBP@Ag nanoparticles with opto-chiral response obtained using gold bipyramids as core. Cysteine, a small thiolated molecule, is used as shaping agent and chiral encoder during the deposition of the Ag or Au metal shell. Cysteine is found to have a strong impact on the morphology in both AuBP@Au and AuBP@Ag systems, preventing the growth of the Ag or Au shell along the longitudinal direction. Moreover, plasmonic circular dichroism is observed for both AuBP@Ag and AuBP@Au systems. The presence of multipolar resonance for AuBPs@Ag suggests that silver is a promising candidate to obtain a strong plasmonic circular dichroism response. Moreover, resonance modes, anisotropy and monodispersity seem relevant conditions to achieve a strong circular dichroism. Concerning the role of cysteine in plasmonic circular dichroism, the crucial importance of the superficial part of the metal shell suggests that the common hypothesis presents in literature could be incomplete. In our system the cysteine entrapped in the interface between the AuBPs and the metal shell, as well as the one encapsulated in the inner metal shell lattice, is not contributing to the plasmonic circular dichroism. These results, supported by theoretical simulations, along with the observed impact of enantiomeric ratio on the final shape, prove that a chiral shape or chiral patterns induced by cysteine during the synthesis in this kind of systems should be taken in consideration. Further investigation will focus on the detailed nanostructure (HRTEM, Electron Tomography), the single object spectroscopy and the localization of the cysteine in the external part of the metal shell.

METHODS

Hexadecyltrimethylammonium bromide (CTAB, 98%, ref. 10146269), tetrachloroauric acid hydrate ($\text{HAuCl}_4 \cdot x\text{H}_2\text{O}$, 99.9%), silver nitrate (AgNO_3 , 99.9995%), and 1,1,3,3-tetramethylguanidine (99%) were purchased from Alfa Aesar. Powder hexadecyltrimethylammonium chloride (CTAC, 98%), sodium borohydride (NaBH_4 , 98%), 8-hydroxyquinoline (99%), catechol (98%), L-ascorbic acid (AA, 99%) from Sigma-Aldrich. Citric acid monohydrate (99.5%) was purchased from Merck. L-cysteine (L-Cys, 98%) was purchased from Acros Organics. D-cysteine (D-Cys, 98%) was purchased from ChemCruz. Sodium hydroxide (NaOH , 97%) and absolute ethanol were purchased from Carlo Erba. All aqueous solutions were prepared in Milli-Q distilled water (18.2 $\text{M}\Omega \cdot \text{cm}$)

Characterization. TEM images were acquired using a JEOL 2100F equipped with a Gatan ultrascan 1000 camera operating at 200 kV while scanning electron microscopy images (SEM) on a MERLIN Compact VP microscope (ZEISS). TEM statistics were acquired measuring over 200 objects with the help of ImageJ software. High-resolution TEM (HRTEM) was performed on a JEOL 2200FS with a point-to-point resolution of 0.23 nm. The extinction spectra were recorded with a PerkinElmer UV-vis-NIR Lambda 750 spectrometer using 1 cm PMMA cuvette for measurements between 350 nm and 1350 nm and quartz 1 mm cuvette for measurements above 1400 nm. Simultaneous measurements of extinction and circular dichroism (CD) spectra were recorded using a J-1700 CD spectrophotometer (JASCO) using 1 cm path PMMA or quartz cuvette. Kuhn's dissymmetry factor (g-factor) was calculated according to the following equation:

$$g\text{-factor} = \frac{CD}{32980 \cdot Ext}$$

With CD in mdeg and Ext the extinction intensities. Dissymmetry g-factor is dimensionless and permits to compare chiroptical activity between different chiral systems.

Synthesis of AuBPs. The AuBPs used as core were prepared according to a protocol fully described by Chateau *et al.*^{37,38} Two main batches of AuBPs were synthesized, AuBP84 and AuBP140 (see [Supporting Information](#) for synthetic details of the AuBPs core).

Synthesis of AuBP@Ag. In a typical synthesis, 20 μL ($[\text{Au}^0] = 0.5 \text{ g/L}$) of AuBP84 or AuBP140 was added in a 4 mL vial containing 1 mL of 30 mM CTAC. Then, 2 μL of L-Cys (10 mM) was added, followed by 100 μL of AgNO_3 (5 mM) and 100 μL of AA (20 mM) and mixed manually to homogenize the mixture. Due to the instability of Cys and AA in diluted aqueous solution, these solutions were prepared and used the same day to improve reproducibility. The mixture was then heated for 30 min in a water bath at 75°C. The color of final suspension was red with an intense yellow scattering. The obtained AuBP@Ag NPs were then washed with water by centrifugation at 8k rpm for 5 min. A final redispersion was done in 1 mM CTAC. To store the NPs, they can be left in the raw reaction mixture and purified when necessary. The particles stored in this condition are stable at least one month after the synthesis.

Synthesis of AuBP@Au. In a 4 mL vial a seed solution was prepared by adding 50 μL ($[\text{Au}^0] = 0.5 \text{ g/L}$) of AuBP140 or AuBP84 to 1 mL aqueous solution of 100 mM CTAB followed by 2 μL of L-Cys (10 mM). In a different vial, the growth solution was prepared adding in the following order, 20 μL of HAuCl_4 (25 mM), 20 μL of AgNO_3 (5 mM) and finally 50 μL of AA (20 mM) to an aqueous solution of 1 mL of 100 mM CTAB at room temperature and mixed manually to homogenize the mixture. Due to the instability of Cys and AA in diluted aqueous solution, these solutions were prepared and used the same day to improve reproducibility. When AA was added, the color of the solution changed from orange/yellow to totally transparent. Then, 1 mL of the growth solution was incorporated in the seed suspension and mixed manually. The mixture was then heated in a water bath for 1 h at 70°C to start the reaction. The color of the final suspension was violet with an intense red scattering. The obtained AuBP@Au NPs were then purified by centrifugation at 8k rpm for 5 min twice and redispersed in 1 mL of 5 mM CTAB. The particles remained stable at least during one month after purification.

Synthesis of AuBP140@AgL@AgD. A volume of 30 μL of AuBP140 ($[\text{Au}^0] = 0.5 \text{ g/L}$) was added in a 4 mL vial containing 1 mL of 30 mM CTAC. Then, 2 μL of L-Cys (10 mM) was added, followed by 100 μL of AgNO_3 (5 mM) and 100 μL of AA (20 mM) at room temperature and mixed manually to homogenize the mixture. The mixture was then heated in a water bath for 30 min at 75°C. The obtained AuBP140@AgL were then washed by centrifugation (8k rpm, 5 min) three times to remove all the excess of L-Cys still present in the solution and finally redispersed in 1 mL of 30 mM CTAC. Then, 2 μL of D-Cys (10 mM) was

added, followed by 100 μL of AgNO_3 (5 mM) and 100 μL of AA (20 mM). The obtained AuBP140@AgL@AgD NPs were then purified by centrifugation and redispersed in 1 mM CTAC.

AuBP84@Au etching. After the synthesis in the conditions described above, AuBP84@Au were purified by centrifugation and redispersed in 2 ml of CTAB (5 mM). To etch them, 1 mL of the suspension was introduced in a 4 mL vial containing 1 mL of CTAB (5 mM) and 2 μL HAuCl_4 (6.25 mM) and incubated for 10 minutes at room temperature (mild conditions). The CD and extinction spectra were then measured. 15 min after the first HAuCl_4 addition, 6 μL of HAuCl_4 was added and the mixture was heated in an oven for 10 min at 45°C (harsh conditions). The CD and extinction spectra were then acquired.

Computational details. Computations were performed using the MNPBEM toolbox of Matlab,⁵⁸ an implementation of the Boundary Element Method (BEM) developed specifically for metal nanoparticles.⁵⁹ This approach, employing classical electrodynamics, has been proven very effective for simulation of AuBPs (obtained from pentatwinned seeds) optical properties, as demonstrated in a previous work.⁶⁰ Here, our previous modeling strategy is extended to model the AuBP140@Ag nanoparticles with 5-fold symmetry bipyramidal outer Ag shell, *i.e.* nano-objects obtained for [Cys] ranging from 5 μM to 100 μM . We used two nested surface meshes: an inner surface representing the Au pentatwinned core and an outer surface representing the silver shell. The surface tip of the outer shell is cut off to leave an Au-exposed tip, as indicated by TEM images of these objects, in such a way that the inner and outer surface meshes are distant enough to avoid numerical errors due to diverging matrix elements. Regarding this last point, we also tested how the tips geometrical features affect the optical response of the overall system and it turned out that they do not significantly affect it (Figure S6). The dielectric functions of Au and Ag are taken from P. B. Johnson and R. W. Christy⁶¹ and the refractive index of the surrounding medium was set to 1.33 (bulk water). The geometrical data of the AuBP140@Ag model structure have been extracted from one measured reference particle observed on the TEM image of the samples with [Cys] of 20 μM and 20 μL of AuBPs. The height of the NPs was set at 134 nm, while the width of the outer shell and inner core at 99 and 32 nm respectively. Starting from this reference model, analogous models have been constructed to simulate the effect of aspect ratio change (with various base sizes at constant length, as documented in the Supporting Information, Figure S7). The quantities computed are the extinction cross-sections to simulate the extinction spectra and the surface charge distributions at given energies, allowing visualization of the excitation character. Additional structures, whose dimensions were chosen to account for the whole statistical distribution in TEM images of the 20 μL sample (Figure 4d), were tested as well (Figure S15) and they showed no significant deviations.

A similar modelling strategy has been adopted for AuBP84Au, where the detailed geometrical parameters of the inner/outer structures can be found in Figure 6b and the related simulations are reported in Figure S17.

In order to perform a qualitative test of the role of surface chirality, a chiral asymmetry is induced artificially, thickening the mesh density around a spiral pattern onto the surface of the object (Figure 5d). This is not geometrical chirality, but it allows to introduce it regardless of the symmetrical features of the model. The simulated CD spectra have been computed using the difference in extinction cross-sections of left-handed and right-handed circularly polarized light. The additional structures based on TEM statistical analysis previously mentioned were also tested for surface chirality (Figure S16).

ACKNOWLEDGMENT

A.C. was supported primarily by the French Minister of Research (MESR) through Ecole Normale Supérieure de Lyon for the PhD project. This work was also supported by Ecole Normale Supérieure de Lyon through a “Projet Emergent” grant and by the ANR through the JCJC grant “PlaChIS” (ANR-20-CE09-0020). The authors would also like to thank PLACAMAT (UMS 3626) for its electron microscopy facilities. I.R. acknowledges the use of HPC resources of the “Pôle Scientifique de Modélisation Numérique”, PSMN at the ENS Lyon, France.

SUPPORTING INFORMATION AVAILABLE

Supporting Information: Additional experimental details, including electron microscopy images, methods and spectra.

REFERENCES

- (1) Ben-Moshe, A.; Maoz, B. M.; Govorov, A. O.; Markovich, G. Chirality and Chiroptical Effects in Inorganic Nanocrystal Systems with Plasmon and Exciton Resonances. *Chem. Soc. Rev.* **2013**, *42*, 7028–7041.

- (2) Ma, W.; Xu, L.; de Moura, A. F.; Wu, X.; Kuang, H.; Xu, C.; Kotov, N. A. Chiral Inorganic Nanostructures. *Chem. Rev.* **2017**, *117*, 8041–8093.
- (3) Ni, B.; Cölfen, H. Chirality Communications between Inorganic and Organic Compounds. *SmartMat* **2021**, *2*, 17–32.
- (4) Hentschel, M.; Schäferling, M.; Duan, X.; Giessen, H.; Liu, N. Chiral Plasmonics. *Sci. Adv.* **2017**, *3*, e1602735.
- (5) Hu, Z.; Meng, D.; Lin, F.; Zhu, X.; Fang, Z.; Wu, X. Plasmonic Circular Dichroism of Gold Nanoparticle Based Nanostructures. *Adv. Opt. Mat.* **2019**, *7*, 1801590.
- (6) Urban, M. J.; Shen, C.; Kong, X.-T.; Zhu, C.; Govorov, A. O.; Wang, Q.; Hentschel, M.; Liu, N. Chiral Plasmonic Nanostructures Enabled by Bottom-Up Approaches. *Annu. Rev. Phys. Chem.* **2019**, *70*, 275–299.
- (7) Cao, Z.; Gao, H.; Qiu, M.; Jin, W.; Deng, S.; Wong, K.-Y.; Lei, D. Chirality Transfer from Sub-Nanometer Biochemical Molecules to Sub-Micrometer Plasmonic Metastructures: Physiochemical Mechanisms, Biosensing, and Bioimaging Opportunities. *Adv. Mater.* **2020**, *32*, 1907151.
- (8) Wen, Y.; He, M.-Q.; Yu, Y.-L.; Wang, J.-H. Biomolecule-Mediated Chiral Nanostructures: A Review of Chiral Mechanism and Application. *Adv. Colloid and Interface Sci.* **2021**, *289*, 102376.
- (9) Zheng, G.; He, J.; Kumar, V.; Wang, S.; Pastoriza-Santos, I.; Pérez-Juste, J.; Liz-Marzán, L. M.; Wong, K.-Y. Discrete Metal Nanoparticles with Plasmonic Chirality. *Chem. Soc. Rev.* **2021**, *50*, 3738–3754.
- (10) Yeom, B.; Zhang, H.; Zhang, H.; Park, J. I.; Kim, K.; Govorov, A. O.; Kotov, N. A. Chiral Plasmonic Nanostructures on Achiral Nanopillars. *Nano Lett.* **2013**, *13*, 5277–5283.
- (11) Singh, J. H.; Nair, G.; Ghosh, A.; Ghosh, A. Wafer Scale Fabrication of Porous Three-Dimensional Plasmonic Metamaterials for the Visible Region: Chiral and Beyond. *Nanoscale* **2013**, *5*, 7224–7228.
- (12) Slocik, J. M.; Govorov, A. O.; Naik, R. R. Plasmonic Circular Dichroism of Peptide-Functionalized Gold Nanoparticles. *Nano Lett.* **2011**, *11*, 701–705.
- (13) Lu, F.; Tian, Y.; Liu, M.; Su, D.; Zhang, H.; Govorov, A. O.; Gang, O. Discrete Nanocubes as Plasmonic Reporters of Molecular Chirality. *Nano Lett.* **2013**, *13*, 3145–3151.
- (14) Yan, W.; Xu, L.; Xu, C.; Ma, W.; Kuang, H.; Wang, L.; Kotov, N. A. Self-Assembly of Chiral Nanoparticle Pyramids with Strong R/S Optical Activity. *J. Am. Chem. Soc.* **2012**, *134*, 15114–15121.
- (15) Kuzyk, A.; Schreiber, R.; Fan, Z.; Pardatscher, G.; Roller, E.-M.; Högele, A.; Simmel, F. C.; Govorov, A. O.; Liedl, T. DNA-Based Self-Assembly of Chiral Plasmonic Nanostructures with Tailored Optical Response. *Nature* **2012**, *483*, 311–314.
- (16) Lu, J.; Chang, Y.-X.; Zhang, N.-N.; Wei, Y.; Li, A.-J.; Tai, J.; Xue, Y.; Wang, Z.-Y.; Yang, Y.; Zhao, L.; Lu, Z.-Y.; Liu, K. Chiral Plasmonic Nanochains via the Self-Assembly of Gold Nanorods and Helical Glutathione Oligomers Facilitated by Cetyltrimethylammonium Bromide Micelles. *ACS Nano* **2017**, *11*, 3463–3475.
- (17) Bao, Z. Y.; Dai, J.; Zhang, Q.; Ho, K. H.; Li, S.; Chan, C. H.; Zhang, W.; Lei, D. Y. Geometric Modulation of Induced Plasmonic Circular Dichroism in Nanoparticle Assemblies Based on Backaction and Field Enhancement. *Nanoscale* **2018**, *10*, 19684–19691.
- (18) Lee, H.-E.; Ahn, H.-Y.; Mun, J.; Lee, Y. Y.; Kim, M.; Cho, N. H.; Chang, K.; Kim, W. S.; Rho, J.; Nam, K. T. Amino-Acid- and Peptide-Directed Synthesis of Chiral Plasmonic Gold Nanoparticles. *Nature* **2018**, *556*, 360–365.
- (19) Lee, H.-E.; Kim, R. M.; Ahn, H.-Y.; Lee, Y. Y.; Byun, G. H.; Im, S. W.; Mun, J.; Rho, J.; Nam, K. T. Cysteine-Encoded Chirality Evolution in Plasmonic Rhombic Dodecahedral Gold Nanoparticles. *Nat. Commun.* **2020**, *11*, 263.
- (20) Cho, N. H.; Byun, G. H.; Lim, Y.-C.; Im, S. W.; Kim, H.; Lee, H.-E.; Ahn, H.-Y.; Nam, K. T. Uniform Chiral Gap Synthesis for High Dissymmetry Factor in Single Plasmonic Gold Nanoparticle. *ACS Nano* **2020**, *14*, 3595–3602.
- (21) Ahn, H.-Y.; Yoo, S.; Cho, N. H.; Kim, R. M.; Kim, H.; Huh, J.-H.; Lee, S.; Nam, K. T. Bioinspired Toolkit Based on Intermolecular Encoder toward Evolutionary 4D Chiral Plasmonic Materials. *Acc. Chem. Res.* **2019**, *52*, 2768–2783.
- (22) Wang, S.; Zheng, L.; Chen, W.; Ji, L.; Zhang, L.; Lu, W.; Fang, Z.; Guo, F.; Qi, L.; Liu, M. Helically Grooved Gold Nanorods: Controlled Fabrication, Superhelix, and Transcribed Chiroptical Switching. *CCS Chemistry* **2020**, *2*, 2473–2484.
- (23) González-Rubio, G.; Mosquera, J.; Kumar, V.; Pedraza-Tardajos, A.; Llombart, P.; Solís, D. M.; Lobato, I.; Noya, E. G.; Guerrero-Martínez, A.; Taboada, J. M.; Obelleiro, F.; MacDowell, L. G.; Bals, S.; Liz-Marzán, L. M. Micelle-Directed Chiral Seeded Growth on Anisotropic Gold Nanocrystals. *Science* **2020**, *368*, 1472–1477.
- (24) Zhang, N.-N.; Sun, H.-R.; Liu, S.; Xing, Y.-C.; Lu, J.; Peng, F.; Han, C.-L.; Wei, Z.; Sun, T.; Yang, B.; Liu, K. Gold Nanoparticle Enantiomers and Their Chiral-Morphology Dependence of Cellular Uptake. *CCS Chemistry* **2021**, *3*, 773–783.
- (25) Ma, Y.; Cao, Z.; Hao, J.; Zhou, J.; Yang, Z.; Yang, Y.; Wei, J. Controlled Synthesis of Au Chiral Propellers from Seeded Growth of Au Nanoplates for Chiral Differentiation of Biomolecules. *J. Phys. Chem. C* **2020**, *124*, 24306–24314.
- (26) Behar-Levy, H.; Neumann, O.; Naaman, R.; Avnir, D. Chirality Induction in Bulk Gold and Silver. *Adv. Mater.* **2007**, *19*, 1207–1211.
- (27) Durán Pachón, L.; Yosef, I.; Markus, T. Z.; Naaman, R.; Avnir, D.; Rothenberg, G. Chiral Imprinting of Palladium with Cinchona Alkaloids. *Nat. Chem.* **2009**, *1*, 160–164.
- (28) Yutthalekha, T.; Wattanakit, C.; Lapeyre, V.; Nokbin, S.; Warakulwit, C.; Limtrakul, J.; Kuhn, A. Asymmetric Synthesis Using Chiral-Encoded Metal. *Nat. Commun.* **2016**, *7*, 12678.
- (29) Wu, X.; Xu, L.; Ma, W.; Liu, L.; Kuang, H.; Yan, W.; Wang, L.; Xu, C. Gold Core-DNA-Silver Shell Nanoparticles with Intense Plasmonic Chiroptical Activities. *Adv. Funct. Mat.* **2015**, *25*, 850–854.
- (30) Hao, C.; Xu, L.; Ma, W.; Wu, X.; Wang, L.; Kuang, H.; Xu, C. Unusual Circularly Polarized Photocatalytic Activity in Nanogapped Gold–Silver Chiroplasmonic Nanostructures. *Adv. Funct. Mater.* **2015**, *25*, 5816–5822.
- (31) Hao, C.; Xu, L.; Sun, M.; Ma, W.; Kuang, H.; Xu, C. Chirality on Hierarchical Self-Assembly of Au@AuAg Yolk–Shell Nanorods into Core–Satellite Superstructures for Biosensing in Human Cells. *Adv. Funct. Mat.* **2018**, *28*, 1802372.

- (32) Hou, S.; Yan, J.; Hu, Z.; Wu, X. Enhancing the Plasmonic Circular Dichroism by Entrapping Chiral Molecules at the Core–Shell Interface of Rod-Shaped Au@Ag Nanocrystals. *Chem. Commun.* **2016**, *52*, 2059–2062.
- (33) Yan, J.; Chen, Y.; Hou, S.; Chen, J.; Meng, D.; Zhang, H.; Fan, H.; Ji, Y.; Wu, X. Fabricating Chiroptical Starfruit-like Au Nanoparticles via Interface Modulation of Chiral Thiols. *Nanoscale* **2017**, *9*, 11093–11102.
- (34) Zheng, G.; Bao, Z.; Pérez-Juste, J.; Du, R.; Liu, W.; Dai, J.; Zhang, W.; Lee, L. Y. S.; Wong, K.-Y. Tuning the Morphology and Chiroptical Properties of Discrete Gold Nanorods with Amino Acids. *Angew. Chem. Int. Ed.* **2018**, *57*, 16452–16457.
- (35) Wang, Y.; He, W.; Li, C. H.; Xia, C.; Yan, Y.; Li, C. M.; Huang, C. Z. Chirality Transfer of Cysteine to the Plasmonic Resonance Region through Silver Coating of Gold Nanobipyramids. *Chem. Commun.* **2021**, *57*, 3211–3214.
- (36) Kotov, N. A.; Liz-Marzán, L. M.; Weiss, P. S. Chiral Nanostructures: New Twists. *ACS Nano* **2021**, *15*, 12457–12460.
- (37) Chateau, D.; Desert, A.; Lerouge, F.; Landaburu, G.; Santucci, S.; Parola, S. Beyond the Concentration Limitation in the Synthesis of Nanobipyramids and Other Pentatwinned Gold Nanostructures. *ACS Appl. Mater. Interfaces* **2019**, *11*, 39068–39076.
- (38) Chateau, D.; Liotta, A.; Vadcard, F.; Navarro, J. R. G.; Chaput, F.; Lermé, J.; Lerouge, F.; Parola, S. From Gold Nanobipyramids to Nanojavelins for a Precise Tuning of the Plasmon Resonance to the Infrared Wavelengths: Experimental and Theoretical Aspects. *Nanoscale* **2015**, *7*, 1934–1943.
- (39) Hu, Z. J.; Hou, S.; Ji, Y. L.; Wen, T.; Liu, W. Q.; Zhang, H.; Shi, X. W.; Yan, J.; Wu, X. C. Fast Characterization of Gold Nanorods Ensemble by Correlating Its Structure with Optical Extinction Spectral Features. *AIP Adv.* **2014**, *4*, 117137.
- (40) Zhuo, X.; Zhu, X.; Li, Q.; Yang, Z.; Wang, J. Gold Nanobipyramid-Directed Growth of Length-Variable Silver Nanorods with Multipolar Plasmon Resonances. *ACS Nano* **2015**, *9*, 7523–7535.
- (41) Yang, Y.; Song, L.; Huang, Y.; Chen, K.; Cheng, Q.; Lin, H.; Xiao, P.; Liang, Y.; Qiang, M.; Su, F.; Chen, T. Asymmetrical Molecular Decoration of Gold Nanorods for Engineering of Shape-Controlled AuNR@Ag Core–Shell Nanostructures. *Langmuir* **2019**, *35*, 16900–16906.
- (42) Goldmann, C.; De Frutos, M.; Hill, E. H.; Constantin, D.; Hamon, C. Symmetry Breaking in Seed-Mediated Silver Nanorod Growth Induced by Dimethyl Sulfoxide. *Chem. Mater.* **2021**, *33*, 2948–2956.
- (43) Haidar, I.; Day, A.; Decorse, P.; Lau-Truong, S.; Chevillot-Biraud, A.; Aubard, J.; Félidj, N.; Boubekeur-Lecaque, L. Tailoring the Shape of Anisotropic Core–Shell Au–Ag Nanoparticles in Dimethyl Sulfoxide. *Chem. Mater.* **2019**, *31*, 2741–2749.
- (44) Lee, J.-H.; Gibson, K. J.; Cheng, G.; Weizmann, Y. Bipyramid-Templated Synthesis of Monodisperse Anisotropic Gold Nanocrystals. *Nat. Commun.* **2015**, *6*, 7571.
- (45) Kou, X.; Zhang, S.; Yang, Z.; Tsung, C.-K.; Stucky, G. D.; Sun, L.; Wang, J.; Yan, C. Glutathione- and Cysteine-Induced Transverse Overgrowth on Gold Nanorods. *J. Am. Chem. Soc.* **2007**, *129*, 6402–6404.
- (46) Wang, W.; Erofeev, I.; Nandi, P.; Yan, H.; Mirsaidov, U. Evolution of Anisotropic Arrow Nanostructures during Controlled Overgrowth. *Adv. Funct. Mat.* **2021**, *31*, 2008639.
- (47) Liu, H.; Li, Z.; Yan, Y.; Zhao, J.; Wang, Y. Silver-Mediated Growth of Chiral Ag/Au-Cysteine Hybrid Nanospheres with Giant Chiroptical Response. *Part. Part. Syst. Charact.* **2020**, *37*, 1900338.
- (48) Schnepf, M. J.; Mayer, M.; Kuttner, C.; Tebbe, M.; Wolf, D.; Dulle, M.; Altantzis, T.; Formanek, P.; Förster, S.; Bals, S.; König, T. A. F.; Fery, A. Nanorattles with Tailored Electric Field Enhancement. *Nanoscale* **2017**, *9*, 9376–9385.
- (49) Mun, J.; Rho, J. Importance of Higher-Order Multipole Transitions on Chiral Nearfield Interactions. *Nanophotonics* **2019**, *8*, 941–948.
- (50) Mun, J.; Rho, J. Surface-Enhanced Circular Dichroism by Multipolar Radiative Coupling. *Opt. Lett., OL* **2018**, *43*, 2856–2859.
- (51) Wu, T.; Zhang, W.; Wang, R.; Zhang, X. A Giant Chiroptical Effect Caused by the Electric Quadrupole. *Nanoscale* **2017**, *9*, 5110–5118.
- (52) Govorov, A. O.; Fan, Z. Theory of Chiral Plasmonic Nanostructures Comprising Metal Nanocrystals and Chiral Molecular Media. *ChemPhysChem* **2012**, *13*, 2551–2560.
- (53) Wang, Y.; Sentosun, K.; Li, A.; Coronado-Puchau, M.; Sánchez-Iglesias, A.; Li, S.; Su, X.; Bals, S.; Liz-Marzán, L. M. Engineering Structural Diversity in Gold Nanocrystals by Ligand-Mediated Interface Control. *Chem. Mater.* **2015**, *27*, 8032–8040.
- (54) Khlebtsov, B. N.; Khlebtsov, N. G. Surface Morphology of a Gold Core Controls the Formation of Hollow or Bridged Nanogaps in Plasmonic Nanomatryoshkas and Their SERS Responses. *J. Phys. Chem. C* **2016**, *120*, 15385–15394.
- (55) Ansar, S. M.; Ameer, F. S.; Hu, W.; Zou, S.; Pittman, C. U.; Zhang, Jr.; Zhang, D. Removal of Molecular Adsorbates on Gold Nanoparticles Using Sodium Borohydride in Water. *Nano Lett.* **2013**, *13*, 1226–1229.
- (56) Khanal, B. P.; Zubarev, E. R. Purification of High Aspect Ratio Gold Nanorods: Complete Removal of Platelets. *J. Am. Chem. Soc.* **2008**, *130*, 12634–12635.
- (57) Lee, Y.-J.; Schade, N. B.; Sun, L.; Fan, J. A.; Bae, D. R.; Mariscal, M. M.; Lee, G.; Capasso, F.; Sacanna, S.; Manoharan, V. N.; Yi, G.-R. Ultraspherical, Highly Spherical Monocrystalline Gold Particles for Precision Plasmonics. *ACS Nano* **2013**, *7*, 11064–11070.
- (58) Hohenester, U.; Trügler, A. MNPBEM – A Matlab Toolbox for the Simulation of Plasmonic Nanoparticles. *Comput. Phys. Commun.* **2012**, *183*, 370–381.
- (59) García de Abajo, F. J.; Howie, A. Retarded Field Calculation of Electron Energy Loss in Inhomogeneous Dielectrics. *Phys. Rev. B* **2002**, *65*, 115418.

- 566 (60) Marcheselli, J.; Chateau, D.; Lerouge, F.; Baldeck, P.; Andraud, C.; Parola, S.; Baroni, S.; Corni, S.; Garavelli, M.; Rivalta,
567 I. Simulating Plasmon Resonances of Gold Nanoparticles with Bipyrnidal Shapes by Boundary Element Methods. *J.*
568 *Chem. Theory Comput.* **2020**, *16*, 3807–3815.
- 569 (61) Johnson, P. B.; Christy, R. W. Optical Constants of the Noble Metals. *Phys. Rev. B* **1972**, *6*, 4370–4379.
- 570